CHAPTER THREE

Cytoskeletal Reorganization of Red Blood Cell Shape: Curling of Free Edges and Malaria Merozoites

Doron Kabaso,[1,2,*] Roie Shlomovitz,[1] Thorsten Auth,[3] Virgilio L. Lew,[4] *and* Nir S. Gov[1]

Contents

Abstract

Human red blood cells (RBCs) lack the actin–myosin–microtubule cytoskeleton that is responsible for shape changes in other cells. Nevertheless, they can display highly dynamic local deformations in response to external perturbations,

* Corresponding author: Tel.: +386 1 476 88 25; Fax: +386 1 476 88 50.
E-mail address: doron.kabaso@fe.uni-lj.si

[1] Department of Chemical Physics, Weizmann Institute of Science, Rehovot, Israel
[2] Laboratory of Biophysics, University of Ljubljana, Ljubljana, Slovenia
[3] Institute for Solid State Research, Research Centre Jülich, Jülich, Germany
[4] Department of Physiology, Development and Neuroscience, University of Cambridge, Cambridge, United Kingdom

Advances in Planar Lipid Bilayers and Liposomes, Volume 13
ISSN 1554-4516, DOI: 10.1016/B978-0-12-387721-5.00003-1

such as those that occur during the process of apical alignment preceding merozoite invasion in malaria. Moreover, after lysis in divalent cation-free media, the isolated membranes of ruptured ghosts show spontaneous inside-out curling motions at the free edges of the lytic hole, leading to inside-out vesiculation. The molecular mechanisms that drive these rapid shape changes are unknown. Here, we propose a molecular model in which the spectrin filaments of the RBC cortical cytoskeleton control the sign and dynamics of membrane curvature depending on two types of spectrin filaments. Type I spectrin filaments that are grafted at one end, or at both ends but not connected to the rest of the cytoskeleton, induce a concave spontaneous curvature. Type II spectrin filaments that are grafted at both ends to the cytoskeleton induce a local convex spontaneous curvature. Computer simulations of the model reveal that curling, as experimentally observed, can be obtained either by an overall excess of type I filaments throughout the cell, or by the flux of such filaments toward the curling edges. Divalent cations have been shown to arrest the curling process and Ca^{2+} ions have also been implicated in local membrane deformations during merozoite invasion. These effects can be replicated in our model by attributing the divalent cation effects to increased filament membrane binding. This process converts the curl-inducing loose filaments into fully bound filaments that arrest curling. The same basic mechanism can be shown to account for Ca^{2+}-induced local and dynamic membrane deformations in intact RBCs. The implications of these results in terms of RBC membrane dynamics under physiological, pathological, and experimental conditions are discussed.

1. Curling of Red Blood Cell Shape

The cortical cytoskeleton of red blood cells (RBCs) is a two-dimensional network of spectrin filaments attached to the internal domain of integral membrane proteins through a variety of intermediate protein links [1]. Under physiological conditions, the spectrin network plays a crucial role in maintaining the normal biconcave shape of the RBC, which allows RBCs to deform and pass through narrow capillaries in the microcirculation. Spectrin network is also essential to stabilize the spiculated RBC shape [2–5]. A dramatic example of cytoskeleton-driven local dynamic membrane shape changes is that documented during the process of spontaneous inside-out membrane curling and eventual vesiculation following cell lysis [6,7]. The unique feature of this process, which makes it an ideal system for studying the molecular mechanism that drives the local shape dynamics of the RBC membrane, is that it operates in a total absence of cytosolic components and external sources of energy, in distilled water media with no divalent cations, and only a trace of a proton buffer. After lysis is completed, the membrane at the free edge of the lytic hole is observed to curl outward in a process that takes several seconds at 37 °C [6]. Our basic

assumption in this study is that the spontaneous curvature of the cell membrane is determined by the anchoring of the spectrin filaments, and therefore connects the molecular (tens of nanometers) and the cellular (several micrometers) length scales. Our model explains how the cortical cytoskeleton can control membrane conformations locally or globally. The model is applied to investigate the curling of isolated RBC membranes and the potential role of Ca^{2+} in arresting curling and mediating localized dynamic membrane deformations in intact RBCs.

2. Cytoskeleton-Induced Membrane Curvature

Curling and subsequent vesiculation of the membrane at the lytic hole have been suggested to correlate with the presence of the spectrin cytoskeleton at the inner membrane surface [6]. After vesiculation is complete, the spectrin actin cytoskeleton detaches and all spontaneous membrane motion ceases [8,9]. The curling phenomenon is not unique to RBCs; images of curled open membranes have been observed in membrane preparations from yeast and other mammalian cells under different experimental conditions [10], suggesting that cortical cytoskeleton components of eukaryotic cells can generate and sustain similar open membrane configurations. Under most experimental conditions, however, a lytic hole in any cell or in a protein-free synthetic lipid bilayer rapidly reseals [6,9,11,12]. In the case of RBCs, the free edge eventually fuses to form cylindrical and spherical multilayered vesicles [6]. Any source of spontaneous curvature in the membranes [13–18] will induce the observed curling, as we demonstrate in our simulations below. The experimental evidence in favor of this curvature being induced by the spectrin cytoskeleton is based on the following points: As long as the spontaneous curling of the free edges proceeds, there will be no release of spectrin–actin to the medium. Spectrin–actin is suddenly released only after vesiculation is completed and the vesicles display retention of sealing markers [9]. In addition, the spectrin filaments are adsorbed only on the inner side of the membrane and this asymmetry is maintained throughout the curling process (see Fig. 2B). Divalent cations arrest the curling process at any intermediate stage of the vesiculation process and also block spectrin–actin release [9]. Lysing of red cells in media with higher ionic strength and osmolality than used for spontaneous vesiculation (1–2 mM Na HEPES, pH 7.5, 0.1 mM EDTA) allows for slow spectrin–actin dissociation with minimal or no spontaneous vesiculation [1,8,20,21]. Under these conditions, the membrane has the appearance of a giant liposome with invisible opening, devoid of any spontaneous motion, and vesiculation of such spectrin-free liposomes can only be induced by the application of vigorous shearing forces [21].

Collectively, this evidence documents a strong association of spectrin–actin with curls and motion. Although it does not directly demonstrate that spectrin filaments drive the curling, it shows that the physical properties of the spectrin–actin-free membrane are not compatible with the detectable spontaneous curling motion.

The spectrin filaments of the cytoskeleton are mostly in the form of tetramers that form a triangular network, with the ends of the tetramers connected to the membrane through actin–band 4 complexes (the vertices of the network). Additionally, the tetramers are randomly anchored to the membrane at their midpoints by ankyrin–band 3 complexes. For simplicity, we neglect the ankyrin anchor complexes and treat the spectrin tetramers as single filaments that can be anchored with only one end attached (type I) or with both ends attached (type II; Fig. 1). Dynamic dissociation and rebinding have been proposed to explain membrane fluctuations and remodeling

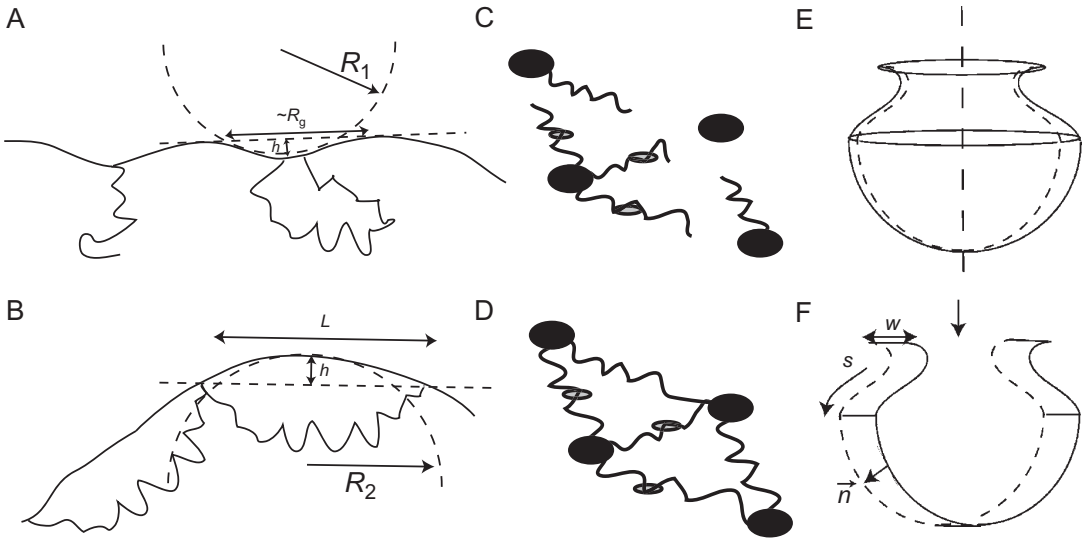

Figure 1 Schematic picture of the spontaneous curvature of the two types of spectrin filaments on the RBC membrane (adapted from Ref. [19]). (A) Type I spectrin filaments that are grafted at one end (left), or at both ends but not connected to the stretched network, induce a concave spontaneous curvature of radius R_1 (R_g is the radius of gyration of the filament). (B) Type II spectrin filaments that are grafted at both ends and are part of the connected stretched network that spans the RBC membranes inner surface (L is the separation between anchoring complexes) induce a local convex spontaneous curvature of radius R_2. An illustration of type I (C) and type II (D) filaments as part of a triangular network in which each edge represents a spectrin tetramer that can be connected to the membrane through actin–band 4 complexes (black circles) and can be further connected to the membrane through band 3 complexes (gray circles) is shown. In (C), the spectrin tetramers are anchored to membrane complexes only at one end (type I), whereas in (D) the spectrin tetramers are anchored at both ends and are part of the stretched network (type II). (E) Schematic illustration of the curling RBC ghost, which has a cylindrical symmetry, and the thin-strip approximation (F) that is used in our calculation. The strip has width w and a contour defined by the coordinate s, and the forces act everywhere along the local normal $\vec{n}$.

of the membrane after the solid-to-fluid transition of a cytoskeletal network [22,23]. Types I and II may be considered symbolic representations for alternative configurations of cytoskeletal components whose interplay can control dynamic changes in membrane curvature. This is the essential mechanistic content of our model. It has been shown both experimentally [24–27] and theoretically [28–30] that a polymer anchored with one end to a lipid bilayer, corresponding to type I spectrin filaments, exerts an entropic pressure such that the membrane curves away from the filament (defined here as a concave local shape with the normal pointing outward from the cell). The thermal fluctuations of the filaments are the source of this pressure and their configuration space is confined by the bounding membrane. This configuration space, and therefore the entropy, increases if the membrane bends away from the type I spectrin filament, thereby allowing more degrees of freedom for the filaments to explore different. The filament pulls the membrane at its anchor and pushes everywhere else. For a membrane patch of size πR_g^2, where the radius of gyration of the spectrin tetramer is $R_g = 13$ nm [31] and a membrane bending rigidity $\kappa = 10 k_B T$, we estimate the induced curvature radius [32] to be $R_1 = 0.1$–1 μm for type I filaments (depending on the spectrin density and anchoring topology; see Fig. 1A). Type II filaments within the intact cytoskeleton network act as stretched entropic springs that locally curve the membrane toward the filament (defined here as a convex shape), as shown in Fig. 1. The finite distance between the spectrin cytoskeleton and the lipid bilayer [33], and the stretched spectrin bonds [34], determines the curvature imposed by the entropic pressure of type II filaments. Since in a disrupted network the anchor distance is unknown, we estimate the entropic effect of the filaments on the membrane curvature to be similar for both types of filaments, but with opposite sign, that is, $R_2 = -R_1$ 0.1 μm (Fig. 1B).

The curvature induced by the spectrin network has been calculated on the length scale of spectrin mesh size [31], as well as on larger scales [35], and several experiments have demonstrated that anchored polymers can indeed produce a spontaneous curvature of such magnitude [26,27]. Based on these results, we developed a model to explain the membrane dynamics observed in the processes of curling and apical alignment. The basic assumption is that the variation in the concentrations of both types of membrane filaments controls the local membrane curvature in space and time (Fig. 2). Although we explicitly describe membrane dynamics in terms of type I and type II spectrin filaments in our model, the model will also apply when curvature is induced by membrane proteins other than spectrin. Divalent ions, such as Ca^{2+}, have been shown experimentally [9,36–38] to induce a stronger binding of the spectrin filaments to the membrane through their anchoring complexes. Therefore, we could translate the effect of divalent cations in the model as inducing a larger equilibrium fraction of type II filaments over type I filaments.

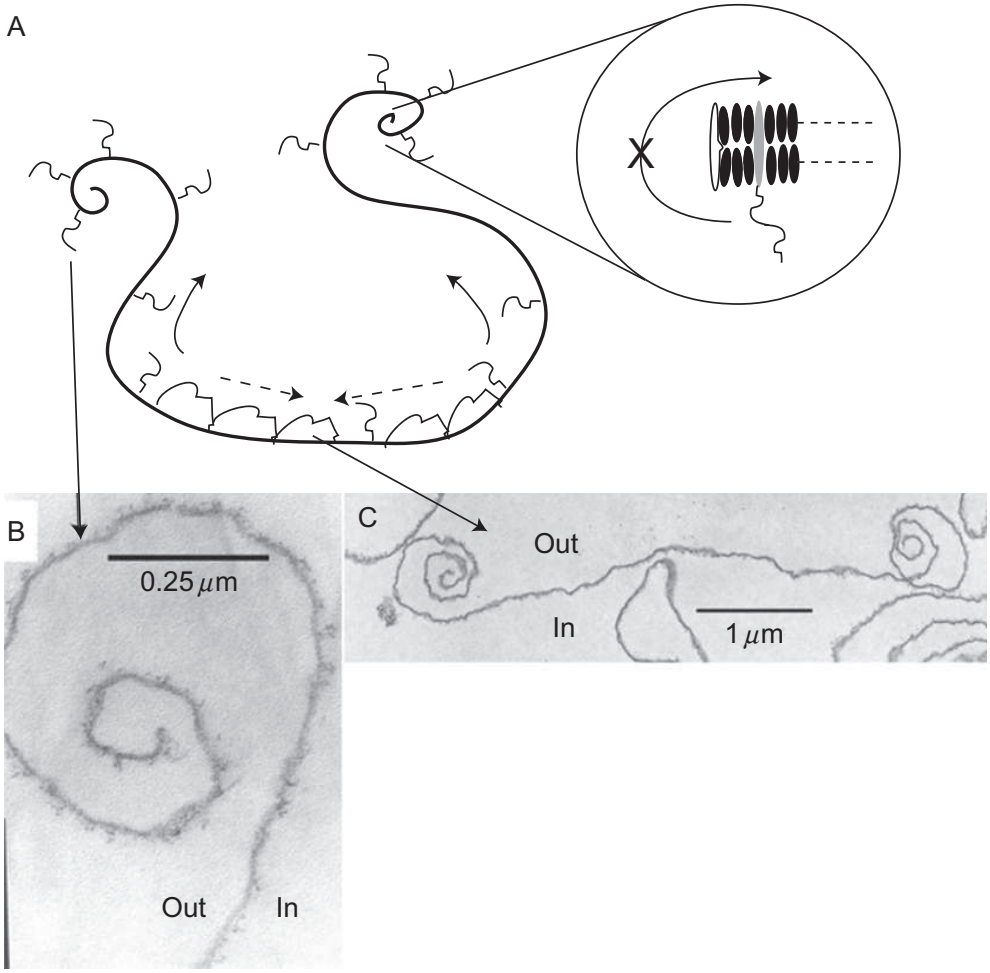

Figure 2 Schematic picture of our model (adapted from Ref. [19]). The connected network of filaments of convex spontaneous curvature (type II) is slowly shrinking and releasing its tension (dashed arrows), slowly squeezing out the type I filaments that have concave spontaneous curvature and migrate (solid arrows) to the curling lip at the open hole. Another mechanism is that rupture of the membrane during hole formation and the consequent curling process convert type II filaments to type I filaments, thereby increasing the overall excess density of type I filaments at the tips and throughout the ghost membrane. These mechanisms are proposed to explain the experimental patterns (A) [6]. In the circled inset is a representation of a type I filament at the hole rim, with lipids as black ovals and transmembrane anchor in gray. The pore edge can be stabilized by curved proteins that are denoted by an open gray shape. The asymmetry between the inner and outer faces of the membrane is maintained because filaments cannot diffuse through the rim to the outer side, and indeed filaments are seen only on the inner side of the membrane throughout the curling process (B). The time period of the curling process is within seconds of membrane rupture [6].

3. The Model for Curling of RBCs

In our model, the densities of both types of spectrin filaments control the membrane curvature (Figs. 1 and 2). We use a continuum model to compute the shape deformation of the membrane and the density

distribution of the two types of filaments. The filament densities are treated as continuum variables, which are the averaged (coarse-grained) values of the discrete distribution of the real filaments. Although we explicitly use type I and type II spectrin filaments as the origin of the curvature, the model also applies when the curvature is induced by membrane proteins other than spectrin, such as curved integral proteins [13,39]. The bending effect of the filaments is treated here with a coarse-grained approach, ignoring the fine-scale wavy nature of the membrane shape due to the anchored filaments [28,31]. The average spontaneous curvature of the membrane is thus induced by the field of filaments. In a dilute regime, where excluded-volume interactions among the filaments are weak, this approach allows us to treat the induced curvature of the two types of filaments in a simple additive manner [40] in the equation for the membrane bending energy (Eq. 1). There are two possible ways to simplify the calculation (1) assume that the membrane deformation and filament distribution are cylindrically symmetric and (2) consider a thin strip of membrane (of width w) that is curved only along its length (while flat along the direction of the strip width—translational symmetry). We followed the second strategy. The Hamiltonian describing the free energy, E, is given by the standard Helfrich-type form [41]:

$$E = \frac{1}{2}\kappa w \int \left(\frac{\partial^2 r}{\partial s^2} - H_1 n_1 - H_2 n_2 \right)^2 \mathrm{d}s, \tag{1}$$

where s is the coordinate along the contour; n_1 and n_2 are the relative densities of the two types of filaments, normalized by the saturating (maximal) packing density of the filaments n_{sat}; κ is the bending rigidity modulus; and $H_1 = 1/R_1$ and $H_2 = 1/R_2$ are the two spontaneous curvatures associated with type I and type II filaments, respectively, so that the overall spontaneous curvature induced by the spectrin filaments is $n_1H_1 + n_2H_2$. This force arises from the mismatch between the local membrane curvature and the local value of the spontaneous curvature (due to the filaments), which drives the membrane to bend so as to reduce the mismatch. Using this free energy, we can now derive the equations of motion for the membrane shape and filament distribution.

Using the calculus of variation (see Supporting Material, Part S1), we derive the following force acting on the membrane in the normal direction, due to the instantaneous distributions of type I and type II filaments:

$$\begin{aligned} F_{\mathrm{n}} = \kappa \Bigg(& \left(\frac{\partial \gamma}{\partial s}\frac{\partial^4 x}{\partial s^4} - \frac{\partial x}{\partial s}\frac{\partial^4 \gamma}{\partial s^4} \right) + \frac{H_1}{2}\frac{\partial^2 n_1}{\partial s^2} + \frac{H_2}{2}\frac{\partial^2 n_2}{\partial s^2} \\ & + (n_1H_1 + n_2H_2)^2 \frac{H}{2} - \frac{3}{2}H^3 \Bigg), \end{aligned} \tag{2}$$

where the membrane curvature is $H = \partial x/\partial s(\partial^2 y/\partial s^2) - \partial y/\partial s(\partial^2 x/\partial s^2)$ (see Supporting Material for the derivation). This force arises from the mismatch between the local membrane curvature and the local value of the spontaneous curvature, which drives the membrane to bend so as to reduce the mismatch. The variation leading to Eq. (2) is a one-dimensional version of the more general expressions derived earlier [42,43]. These expressions recover the familiar form for small undulations of a flat membrane in the Monge gauge. Note that whereas most previous works dealt with the stationary shapes of membranes [42–44], here we are solving the dynamics of the membrane shape deformations. Below, we show that the dynamics is nontrivial; for example, a membrane with a uniform spontaneous curvature is shown to curl from its free edges inward. Details of the simulation techniques are given in the Supporting Material, and here we mention just the main properties. In addition to the curvature-driven forces given by Eq. (2), there are two more forces that act on the membrane in our simulations (1) the stiff harmonic-spring interaction between the nodes along the membrane maintains a constant overall length of membrane strip and (2) an artificial short-range repulsion prevents the membrane from overlapping on itself. The sum of these forces acting on the membrane is then used in the equation of motion of the membrane, which is written in the limit of local hydrodynamic interactions [45]:

$$V_n = F_n \xi, \tag{3}$$

where V_n is the normal velocity of the membrane and ξ is the effective friction coefficient that takes into account the viscous drag exerted by the fluid that surrounds the membrane locally (this is a simplified form of the Oseen tensor in the limit of only short-range hydrodynamic interactions). The full solution of this system, including the hydrodynamic flows around the curling membrane, awaits a future study. Finally, since we work in translational symmetry, the free edges of the membrane strip (the endpoints of our one-dimensional contour) correspond to the membrane edge along the hole in the real ghost. The hole radius and edge length are thus meaningless, and their energy contribution (line tension) is therefore constant. In the real situation, the hole starts from some minimal radius size, which has a large distribution. Nevertheless, the curling process is observed experimentally [6] to proceed without any correlation to the radius of the hole; it is observed to be identical along the edges of both small holes of radius $R \approx 0.5$ μm and large holes of $R \approx 10$ μm (Fig. 2C). We therefore decided to investigate the curling process independently of the issue of hole edge length, as is inherent to our choice of translational symmetry (Supporting Material, Part S2.4). The weak effective line tension observed in the RBC ghosts [6] may arise due to the stabilization of the pore edge by curved membrane proteins (Fig. 2A, inset). The simulations presented here using

translational symmetry are reasonably accurate as long as the hole radius is much larger than the radius of curvature induced by the filaments, that is, $R \gg 0.1$ mm. The boundary conditions at the two free endpoints of the membrane (on both sides of the hole) were set, so that the membrane at the edges would have the curvature imposed by the local filament density (Supporting Material, Part S2.3). The filaments diffuse in the membrane, with conservation of the total number of filaments for each type. For simplicity, we do not allow spontaneous filament-type interconversion although this can easily be added. The membrane conformation acts as a potential landscape in which the two different types of filaments flow. The resulting fluxes of filaments are given in the Supporting Material.

4. Numerical Simulations

4.1. Effects of Filament Type and Density on Membrane Curling Pattern

To isolate the effect of filament types and densities on the membrane dynamics, we ran simulations with only one type of filament (i.e., type I or type II). The filaments in this set of simulations had negligible filament mobility ($n_{sat} = 1000\ \mu m^{-2}$; $\Lambda/n_{sat} = 1 \times 10^{-5}$ g s^{-1}, where Λ is the filament mobility in the membrane). Figure 3A and B shows snapshots of simulations with type II filaments at low and high relative densities. Curling at the free edges is inward, with an outside-in topology (a pattern that has been observed in a synthetic vesicle system [46] but never observed experimentally in RBCs), and the radius of the curled membrane is 0.25 μm and 0.1 μm for the initial relative filament densities of 0.4 and 1, respectively. Note that the curling process starts at the ends of the strip in our simulations, as observed experimentally [6]. This is because the curvature forces are mostly balanced within the bulk of the membrane, leaving the free edge as the only location of unbalanced forces. Mathematically, this can be seen from Eq. (2): For a uniform distribution of one type of filament, the force due to the filaments comes only from the fourth term on the right-hand side. This term is proportional to the membrane curvature, which is initially low everywhere (radius of the ghost membrane) except at the free ends, where the local curvature is defined by the spontaneous curvature of the filaments there (Part S2.3, Eq. S22 of the Supporting Material). The forces at the free ends are therefore dominant and drive the curling from the edges inward.

In Fig. 3C and D, we show the analogous results for type I filaments. Here, we find the same curvature radii of 0.25 and 0.1 μm, but curling is outward, with an inside-out topology. This agrees with the curling observed in the RBC and was also observed in the curling synthetic vesicle

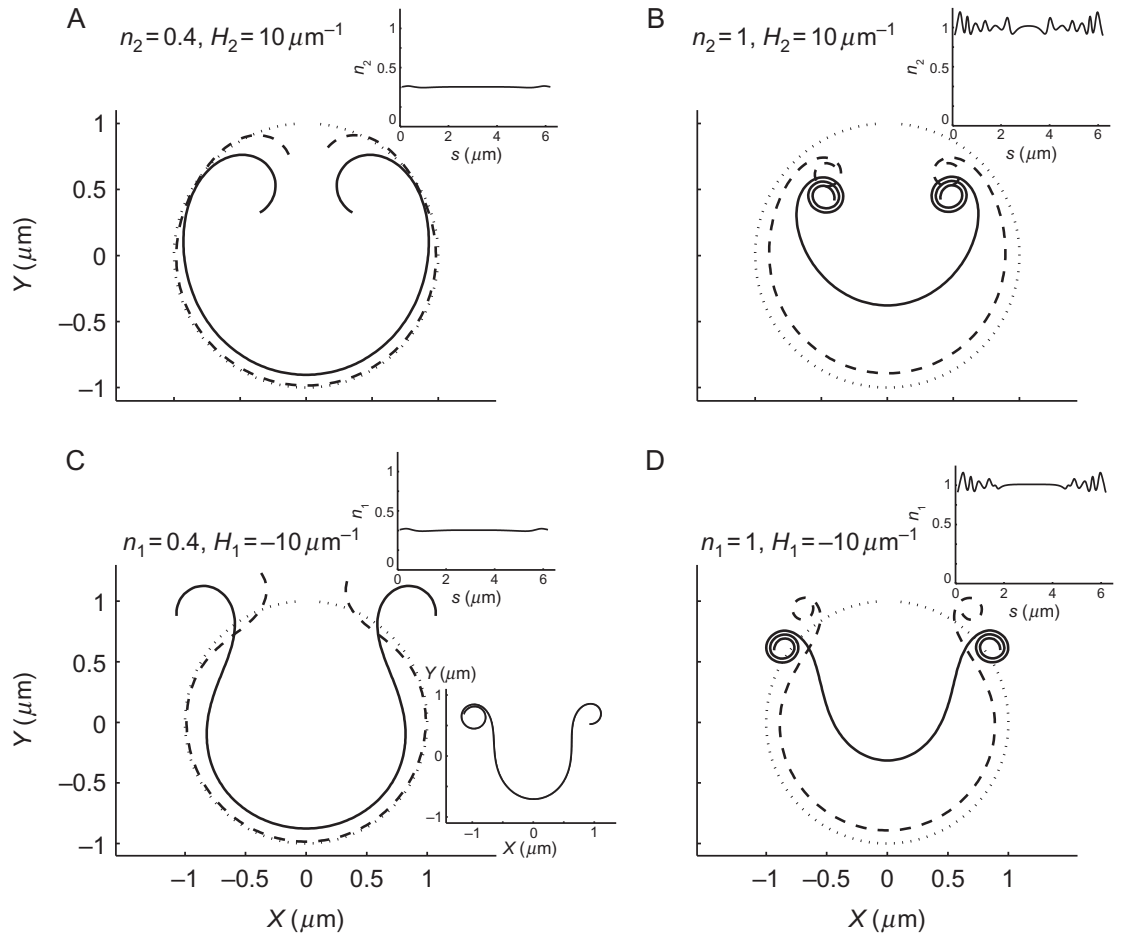

Figure 3 Effects of filament types and densities on the membrane dynamics (adapted from Ref. [19]). The two top panels (A) and (B) describe cases of type II filaments at low and high densities, within 30 s. The curvature sign is positive ($H_2 = 10\ \mu m^{-1}$), and as a result the curling is inward. The two bottom panels (C) and (D) describe cases of type I filaments at low and high densities. The curvature sign is negative ($H_1 = -10\ \mu m^{-1}$), and as a result the observed curling is outward. In all cases, the mobility of the filaments was quite low ($n_{sat} = 1000\ \mu m^{-2}$; $\Lambda/n_{sat} = 1 \times 10^{-5}\ g\ s^{-1}$). The insets at the top of each panel describe the final distribution of the filaments. Since the mobility is low, the final distribution has small fluctuations around the initial uniform spatial distribution. In each panel, the dotted line describes the initial membrane shape of a circle with a hole, the dashed line describes an intermediate time, and the solid line describes the final shape within a time period of 30 s.

system [46]. After 30 s, the membrane has curled three turns for simulations with high filament density, whereas not even a single turn was completed in the simulations at low density. If the simulation in Fig. 3C is allowed to run over a much longer time (90 min), we get curling with more than one turn of the membrane and an even greater radius of curvature ($\approx 0.2\ \mu m$). This greater radius of curvature is due to the flux of filaments toward the edges (results not shown). The high-density case matches the experimentally observed radius of the innermost curl (0.1 μm; Fig. 3D). Note that excluded-volume repulsive forces generate the spiral pattern such that

only the innermost part of the membrane achieves the desired curvature and the rest of the membrane spirals around it with an ever larger radius of curvature. These results show that only the simulations with a high density of type I filaments in the ruptured ghost render the experimentally observed curling pattern of the membrane (Fig. 3D). For a good experimental fit, $>90\%$ of the filaments should be of type I. This suggests that lytic rupture in the unique conditions that trigger spontaneous inside-out vesiculation explosively redistributes the filament distribution from a prelytic state with comparable proportions of type I and type II filaments to a $>90\%$ type I filament excess. Excesses of smaller magnitude would lengthen the curling process and reduce the curvature, and this may also account for some of the experimentally observed variability. Note that the membranes in the experiments evolved further beyond the curling process, by means of a series of cutting–splicing events, so that the curled part of the ghost is finally dashed up into small vesicles [6,7]. These vesicles satisfy the minimum curvature energy requirement as dictated by the density of type I filaments adsorbed on the external surface of the membrane. This step cannot be captured by our simplified calculation using only a thin strip of membrane.

4.2. Effects of the Initial Filament Distribution on the Membrane Curling Pattern

During rupture of the RBC, a higher proportion of type I filaments might be produced close to the lytic hole due to mechanical disruption of the spectrin network. To evaluate the effect of an inhomogeneous initial distribution of the filaments on the membrane dynamics, we ran simulations with asymmetric distributions for both types of filaments. In addition, the diffusion of spectrin filaments with high mobility ($n_{\mathrm{sat}} = 100\ \mu\mathrm{m}^{-2}$; $\Lambda/n_{\mathrm{sat}} = 1 \times 10^{-4}\ \mathrm{g\ s}^{-1}$) was included. The initial distributions had an excess of type I filaments at the free edges, with the excess decaying as a Gaussian from the edges to the middle. We varied the gradient of the filament density by changing the width of the Gaussian distribution. Far from the edges, we assumed that the two types of filaments have equal concentration, as in an intact RBC. The distribution of type I at the edge was set to a density of 0.7 or 0.83 (i.e., an excess amplitude of $\delta = 0.2$ or $\delta = 0.33$, respectively), decaying to a base level of 0.5 with a variance of either $\sigma = 1\ \mu\mathrm{m}^2$ or $\sigma = 6\ \mu\mathrm{m}^2$. The excess of type I filaments results from the detachment of type II filaments, so that an excess of one type occurs at the expense of the other type (conservation of total number of filaments). In Fig. 4, we show the results for different amplitudes and widths of the initial density variation. After 30 s of simulation, the results show that when the amplitude of the normal distribution is $\delta = 0.33$ filaments $\mu\mathrm{m}^{-1}$, $\sigma = 1\ \mu\mathrm{m}^2$ or $\delta = 0.33$ filaments $\mu\mathrm{m}^{-1}$, $\sigma = 6\ \mu\mathrm{m}^2$, the edges deform by half a turn and one complete turn, respectively. We observe that as the

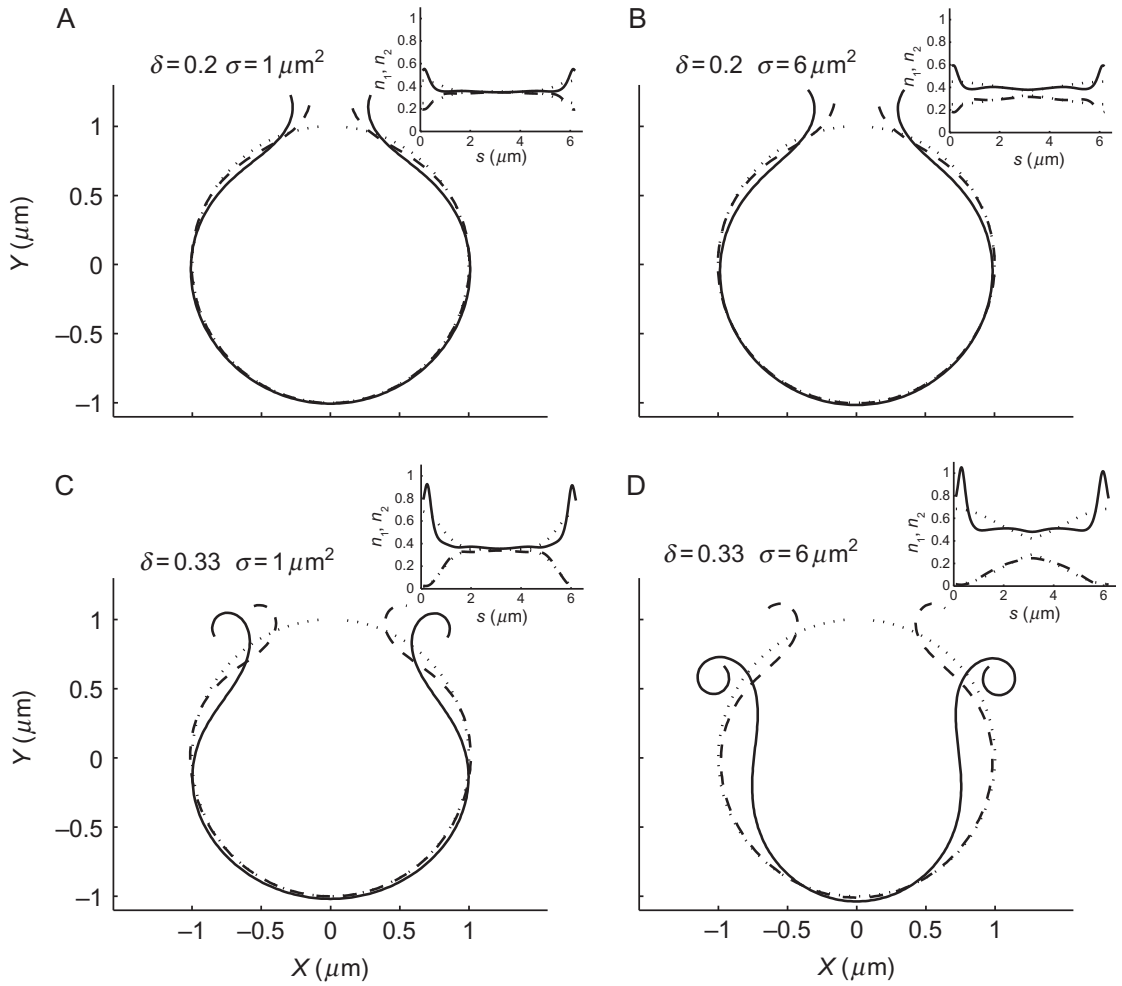

Figure 4 Effects of the spatial distribution of type I and type II filaments on membrane dynamics (adapted from Ref. [19]). The initial distribution has an excess of type I filaments localized at the edges of the hole, with a normal distribution of amplitude (δ) such that the density of the filaments at the edges is $0.35 \pm \delta$ (for type I and type II, respectively). The top and bottom rows are for $\delta = 0.2$ (μm^{-1}) and $\delta = 0.33$ (μm^{-1}), and the left and right columns are for $\sigma = 1$ (μm^2) and $\sigma = 6$ (μm^2), respectively. The mobility of the filaments is quite high ($n_{sat} = 100\ \mu m^{-2}$; $\Lambda/n_{sat} = 1 \times 10^{-4}$ g s^{-1}) in comparison to the low mobility in Fig. 3. Note that for the case of $\delta = 0.2$ (μm^{-1}), this amplitude was not sufficient to curl the membrane within the given time frame of 30 s (A, B). In addition, the case of high amplitude and low variance is not sufficient to form a complete curl. Finally, the case of high amplitude $\delta = 0.33$ (μm^{-1}) and high variance $\sigma = 6$ (μm^2) yields a single curl within 30 s. Note that the larger variance creates a larger pool from which to attract more type I filaments toward the edges (D). In each inset, the dotted lines are the initial distribution of filaments, the dashed line is the distribution of type II filaments, and the solid line is the distribution of type I filaments. In the inset of (D), note the large flux of filament type I toward the edges.

membrane edge curls, this curvature attracts type I filaments, whereas type II filaments are repelled from this region (see distributions of filaments in the insets). We conclude that if the mobility of the filaments is large enough to respond to the membrane curvature with a large flux, as shown in Fig. 4D,

then a relatively moderate excess of type I over type II filaments at the edges of the hole is sufficient to curl the free edges of RBCs to the extent seen in the experiments. If the excess at the edges is too small (Fig. 4A–C), we find that the resultant membrane curling is much smaller compared to that in the experiments. We further conclude that diffusion and segregation of the two filament types are not sufficient by themselves to drive the curling of the whole membrane—a global excess of type I is also required.

4.3. Modeling the Effect of Divalent Ions

The documented Ca^{2+}-induced increase in the binding strength of spectrin filaments to the membrane [38] may be expected to effectively freeze the filament distribution due to a strong decrease in filament mobility, with an ensuing turnover of type I to type II filaments (Eq. S28) and cytoskeletal crosslinking [6]. We found that the curling and spontaneous inside-out vesiculation process could be instantly arrested at any stage by the addition of divalent cations to the medium, but reversibility was observed only with Mg^{2+} ions. In Fig. 5, we model these divalent cation effects under two of the conditions analyzed above (1) low mobility of spectrin filaments and large excess of type I filaments throughout the membrane (as in Fig. 3D) and (2) high-mobility filaments and a localized excess of type I filaments at the free edges (as in Fig. 4D). In the low-mobility case (top row), we simulated the effect of the divalent ions after allowing the membrane to curl freely for 2 s. We first modeled the effect of the ions by elimination of filament diffusion, but this did not stop the curling because the excess of type I filaments was still high enough to keep the process going (Fig. 5A). We next modeled the effect of the ions as a global turnover of type I to type II. We chose a significant turnover of 50% (this value is somewhat arbitrary) of type I to type II due to the addition of the ions and found that this practically arrested the curling process; the spontaneous curvature was reduced significantly (to zero for this choice of parameters) and the curls began to slowly unfold (Fig. 5B).

In the high-mobility and localized excess case (Fig. 5, bottom row), we tested the effects of the divalent ions by elimination of filament diffusion (Fig. 5C) and turnover of type I to type II (Fig. 5D). We found that when the ions diminished the diffusion, the curling process was considerably slowed down (Fig. 5C) compared to the results shown in Fig. 4D. A partial turnover of type I to type II also effectively arrested the curling (Fig. 5D), initiating a partial unfolding of the curls. We conclude that when the mobility of spectrin filaments is high enough to play a role in the curling process, the elimination of diffusion due to the ions will slow down the curling, whereas the turnover of type I to type II filaments due to the addition of ions is always a sufficient mechanism to account for the observed arrest in the curling.

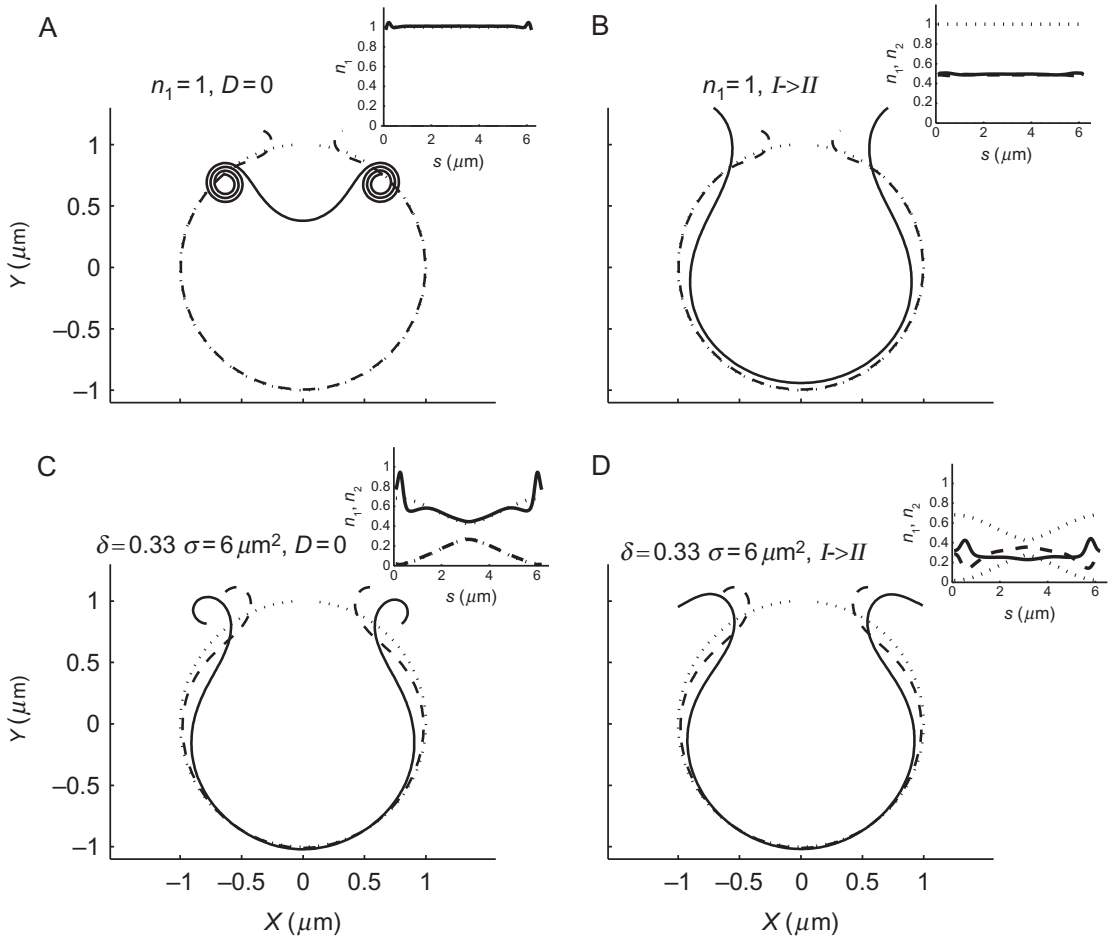

Figure 5 Modeling the effects of adding divalent ions on the membrane dynamics (adapted from Ref. [19]). The addition of divalent ions is modeled by eliminating the diffusion of filaments or by the turnover of type I to type II filaments. This modeling is performed for two successful cases (1) high and uniform density ($n_1 = 1$) of type I filaments with low mobility, as described in Fig. 3D (shown here in the top row) and (2) a more localized spatial distribution with large amplitude and variance ($\delta = 0.33$ (μm^{-1}), $\sigma = 6$ (μm^2)) as described in Fig. 4D (shown here in the bottom row). The results for the arrest of diffusion are demonstrated in the left column, and the results for the partial turnover of type I to type II filaments are demonstrated in the right column. Since the curling in Fig. 3D is obtained within 10 s, the arrest of diffusion is performed after 2 s (A). Note that the arrest of diffusion is not able to stop the curling. In contrast, the curling in Fig. 4D is obtained within minutes, which allows us to arrest the diffusion after 10 s (C). This arrest slows down the curling, and a single full curl is not obtained within the time frame of 30 s. In the right column, the turnover is of 50% of type I into type II filaments, which is sufficient to stop the curling and to even unfold its curled edges (B, D).

5. Malaria Merozoites and Ca^{2+} Dynamics

During the approach of a malaria merozoite to a targeted RBC, the red cell undergoes local and highly dynamic shape changes [47–50]. If the initial contact is away from the apical pole of the merozoite, which is

required for penetration, the RBC responds with rapid merozoite-engulfing motions and the merozoite reorients to achieve apical contact. As soon as this is attained, the RBC returns to its normal biconcave shape and remains quiescent while it is penetrated by the parasite. Immediately after the parasite is internalized, a second and more prolonged wave of dynamic deformations takes place. Ca^{2+} ions have been implicated in both early and late dynamic responses during merozoite invasion [51].

6. The Model for RBC and Malaria Merozoite Interaction Prior to Invasion

The model as described up to now proved sufficient to describe the curling process of RBCs. In the case of the merozoite attachment, only a small patch of the RBC membrane close to the parasite has to be simulated, so we used periodic boundary conditions with increased spatial resolution compared to the simulations for curling. To simulate the effects attributed to Ca^{2+} in the malaria preinvasion events, we incorporated a simplified version of the known pump-leak Ca^{2+} balance across the RBC membrane.

The relation between the local Ca^{2+} concentration and the density of protein filament concentrations was assumed to be described by an instantaneous chemical equilibrium relation:

$$n_1 \rightleftharpoons n_2, \tag{4}$$

where the left and right arrows are for the equilibrium constant k and k', respectively. The two equilibrium constants are

$$\begin{aligned} k &= \exp\left(\frac{\alpha n_{\mathrm{Ca}}}{k_{\mathrm{B}}T}\right), \\ k' &= \exp\left(\frac{-\alpha n_{\mathrm{Ca}}}{k_{\mathrm{B}}T}\right), \end{aligned} \tag{5}$$

where αn_{Ca} represents the Boltzmann energy difference δE. The concentration of the two filament types is determined from

$$\begin{aligned} n_2 &= n_1 \exp\left(\frac{-2\alpha n_{\mathrm{Ca}}}{k_{\mathrm{B}}T}\right), \\ n_1 &= n_{\mathrm{tot}} - n_2, \end{aligned} \tag{6}$$

where the exponential factor is derived from k'/k (Eq. 5) and n_{tot} is the total density of filaments, which equals unity. The local density of type II filaments depends on the local density of Ca^{2+} as follows:

$$n_2 = n_{\mathrm{tot}} \frac{1}{\exp(-0.05 n_{\mathrm{Ca}}) + 1}, \tag{7}$$

where the numerical factor in the exponent gives the Ca^{2+}-induced affinity of spectrin filament binding. The density of Ca^{2+} ions is

$$n_{\mathrm{Ca}} = N_{\mathrm{Ca}}/\mathrm{d}s, \tag{8}$$

where N_{Ca} is the number of Ca^{2+} ions and ds is the distance between consecutive nodes.

The density of Ca^{2+} ions is treated along the membrane and represents those ions that reside within the interaction volume close to the membrane, where they can interact with the spectrin filaments. The thickness of this interaction volume is similar to that of the spectrin network, which is $\sim$30 nm, and its width is simply that of the membrane strip that we are modeling. The influx of Ca^{2+} is assumed to occur only at the region of contact between merozoite coat and RBC membrane, which has a length of 0.5 μm. A single influx pulse of Ca^{2+} is modeled with maximum amplitude of $\sim$600 ions μm^{-3}, to ensure that $n_2 \sim 1$ at the contact region, and is held constant for 2 s. After this time, the amplitude of the pulse decays exponentially by active extrusion and by diffusion away from the contact region along the membrane according to a simple diffusion equation:

$$\frac{\partial N_{\mathrm{Ca}}}{\partial t} = D_{\mathrm{Ca}} \frac{\partial^2 N_{\mathrm{Ca}}}{\partial s^2} - K_{\mathrm{eff}} N_{\mathrm{Ca}} + J_{\mathrm{in}}, \tag{9}$$

where D_{Ca} is the effective diffusion constant for Ca^{2+} ions, K_{eff} is the efflux rate of Ca^{2+} ions, and J_{in} is the influx of Ca^{2+}.

Most of the biophysical parameters used in this work were taken from the literature. The diffusion coefficient of proteins within the membrane was previously estimated to be 0.01–0.005 $\mu m^2\ s^{-1}$ [52], whereas the diffusion coefficient of spectrin filaments was smaller, at 0.001 $\mu m^2\ s^{-1}$ [52]. The bending rigidity is on the order of $10 k_B T$. The only parameter that was fitted to give a good agreement with the experiment was the effective membrane friction in Eq. (3). The efflux of Ca^{2+} was taken as 35 s^{-1} [53] and the diffusion coefficient of Ca^{2+} was estimated at 1 $\mu m^2\ s^{-1}$ [54]. The saturating (maximal packing) density of the filaments, n_{sat}, can be estimated from previous measurements [38] and taken to be on the order 1000 μm^{-2}.

6.1. Modeling the Effects of Ca^{2+}-Dependent Filament Turnover

We next applied our model to simulate the membrane dynamics of an intact RBC in response to a transient local influx of Ca^{2+} ions. Such Ca^{2+} influx transients have been proposed to follow the initial contacts between merozoites and RBCs before merozoite invasion [48,51]. Ca^{2+} influx was simulated by means of a step-function amplitude with a spatial width of 0.5 μm held constant for 2 s. The density of the type I and type II filaments was determined by the local instantaneous Ca^{2+} concentration (see Eq. S28). We chose a 3-μm long membrane for these simulations, using periodic boundary conditions. We assumed that the initial filament density was the same for both species ($n_1 = n_2 = 0.5$). The Ca^{2+} pulse was assumed to cause a complete turnover of type I to type II filaments at the point of maximum amplitude, to give us an estimate of the upper bound of the amplitude of membrane deformation. The results are shown in Fig. 6A and B (Table 1). The Ca^{2+}-induced turnover of type I to type II filaments caused the bending of the initially planar membrane in both the inward and outward directions due to the resulting inhomogeneous spontaneous curvature. The maximal membrane deformation was 0.4 μm after 2 s. In Fig. 6C and D, the Ca^{2+} influx region was held fixed in space and prevented from folding inward. Despite this restriction, the folding outward of the surrounding membrane remained robust. Note that although the adhesion region prevents the membrane from folding inward, the folding outward remains robust (C).

7. Modeling the Egress of Malaria Merozoites

While previous research has shown that proteases induced by the parasite degrade the RBC proteins as well as the cytoskeleton [55–57], we here hypothesize that degradation of the spectrin network stimulates a turnover of type II into type I filaments (Fig. 7). In addition, type I filaments may stabilize membrane pores formed seconds before the lytic stage and the dispersion of packed merozoites. The rapid coalescence of smaller pores into larger pores may be facilitated by increasing densities of type I filaments (Fig. 7). Furthermore, the high densities of type I filaments following the lytic stage could explain the documented outward curling of the RBC membrane. Future modeling and experimental studies are needed to test these ideas.

8. Conclusions

The results presented here show that a model based on the assumption that spectrin filaments attached to the inner side of the lipid bilayer membrane induce a spontaneous curvature can explain local dynamic membrane

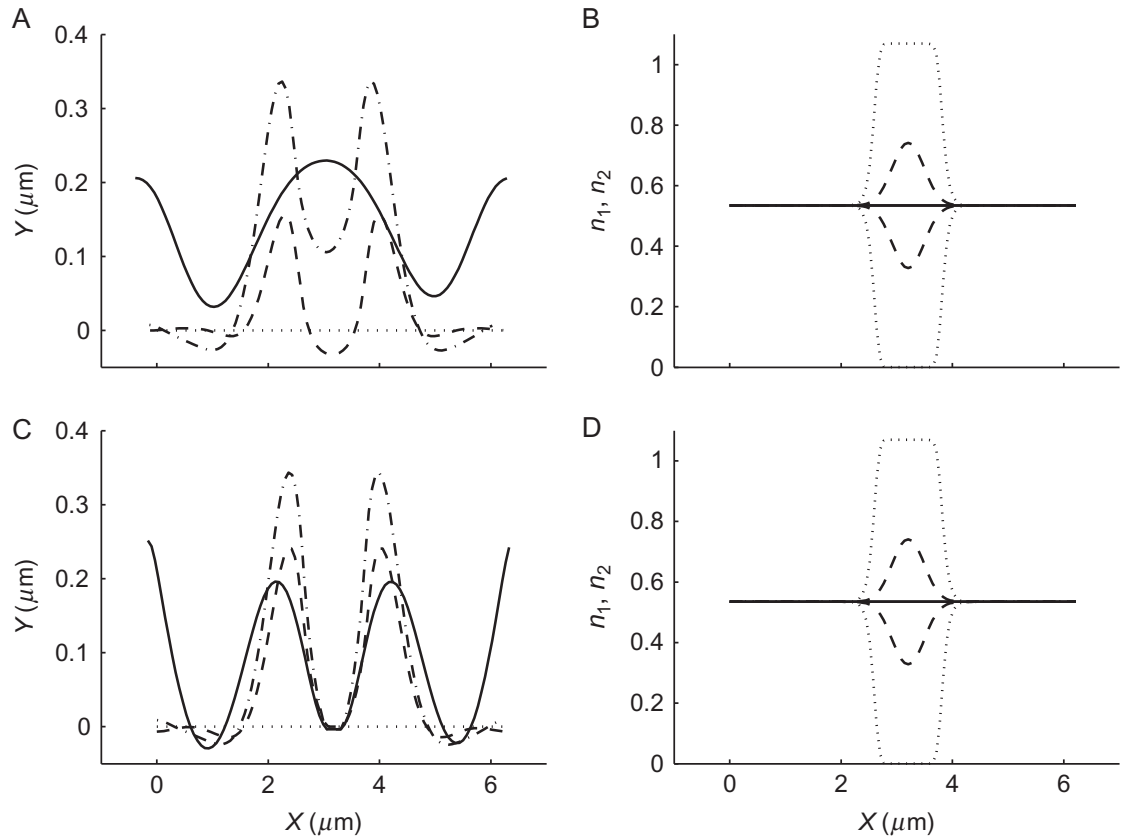

Figure 6 Exploring the effects of a Ca^{2+} influx pulse on local membrane shape in an intact RBC, assuming the same mechanism as that applied to explain curling arrest by divalent cations (adapted from Ref. [19]). Two scenarios are modeled (1) the membrane in the Ca^{2+} influx region is free to move (top row) and (2) it is held fixed (bottom row). The distributions of the two types of filaments are determined by the instantaneous local Ca^{2+} concentration. Therefore, the distribution has an excess of type II over type I filaments at the middle of the membrane. The density distributions of the two types are shown in (B, D). The influx of Ca^{2+} is constant for a period of 2 s and causes the conversion of type I to type II (dotted line in B, D), compared with an initial density of 0.5 for both types of filaments. After 2 s, the influx stops, and as a result the Ca^{2+} density decays within 0.5 s, and consequently the filament densities decay toward 0.5 (dashed line in B, D). The turnover of type I to type II filaments causes the bending of the straight initial membrane (dotted line in A, C) in both the inward and outward directions (D). After 0.5 s, the shape is given by the dashed line (A, C) and the maximal amplitude of 0.4 μm is reached after 2 s (the dotted-dashed line in A, C). The solid line is the shape of the membrane after 10 s. Slow mobility of the filaments is allowed and values are listed in Table 1.

shape changes observed in experiments. Two classes of filaments are considered in the model depending on whether one end (type I) or both ends (type II) of the spectrin tetramer are attached to the membrane. Each type induces a spontaneous curvature on the membrane of opposite sign and roughly equal magnitude. The model treats these nanometer-scale components in a continuum landscape of variable local densities of each filament type in response to environmental conditions and membrane shape. We sought

Table 1 List of parameters used in our simulation study

Curvature, H_1 (μm^{-1})	-10	Temperature, T (K)	300
Curvature, H_2 (μm^{-1})	10	Bending rigidity, κ ($k_B T$)	10
n_1, n_2, relative densities of type I and type II filaments	$\hat{n}_1/n_{sat}$ $\hat{n}_2/n_{sat}$	n_{sat}, maximum number of filaments per micron squared (μm^{-2})	100, 1000
Diffusion coefficient of filaments, D ($\mu m^2\ s^{-1}$)	0.001	Mobility of proteins, Λ ($g\ s^{-1}\ \mu m^{-2}$)	$D/(k_B T)$
Viscosity (water), η ($g\ m^{-1}\ s^{-1}$)	10^{-4}	Relative mobility ($g\ s^{-1}$)	Λ/n_{sat}
Filament length scale, d (μm)	0.1	Oseen tensor ($s\ g^{-1}$)	12.5
Threshold distance for repulsion (μm)	0.0327	D_{Ca} ($\mu m^2\ s^{-1}$)	1
Ca^{2+} efflux rate, K_{eff} (s^{-1})	35		

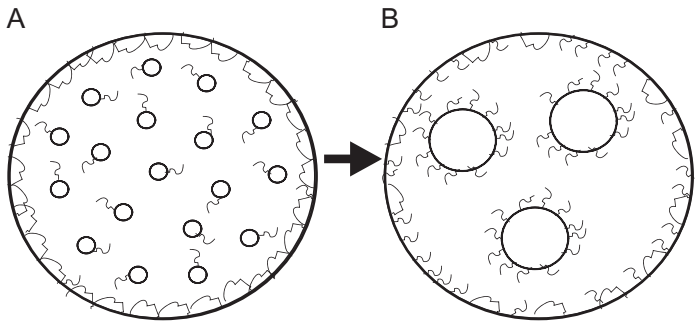

Figure 7 Schematic model for the stabilization and coalescence of membrane pores during egress of malaria parasites. (A) Small membrane pores (inner circles) are formed seconds before the egress and dispersion of malaria parasites. Since the pores are of a negative curvature, they can be stabilized by type I filaments, while type II filaments prefer the positive curvature of the red blood cell membrane (outer circle). (B) Large membrane pores are formed and stabilized by increasing densities of type I filaments. Note that the origin of type I filaments could be due to the degradation of type II filaments by proteases activated by the packed malaria parasites.

to determine whether the model could account for two well-documented examples of dynamic membrane deformations (1) the curling phenomenon of spontaneously vesiculating RBC ghosts and (2) the mechanism of membrane deformation during apical alignment of malaria parasites. In the study of the curling phenomenon, the simulations showed that either an overall excess of type I filaments or an initial excess of type I filaments close to the lytic hole could initiate the outward curling of the cell membrane. Comparing the model with experiment (see Figs. 3–5) allowed us to fit the free parameter of our model, the effective membrane hydrodynamic friction. Divalent cations have been shown to arrest the curling and spontaneous vesiculation process [6,9] and to induce stronger spectrin–membrane binding [37,38]. This effect is represented in the model by the elimination of filament diffusion and a turnover of type I to type II filaments. We find that the cation-induced turnover of type I to type II filaments is the dominant mechanism that allows us to reproduce the experimentally observed arrest of the curling (Fig. 5).

The mechanism of the effects attributed to Ca^{2+} was also investigated in relation to the potential of transient Ca^{2+} influx during merozoite apical alignment [47,48,51,58]. The results (Fig. 6) show that the amplitude and timescale of the membrane deformations induced by the transformation of type I to type II filaments are in good quantitative agreement with those documented in the best available observations of this process [47–49]. In addition, the simulations show that when the cytoskeleton consists mainly of type II filaments, membrane dynamics cannot occur and thus invasion efficiency is reduced. This may help explain the reduced invasion previously observed in ATP-depleted and volume-reduced RBCs [59–61]. The basic idea developed here—that spectrin filaments, or spectrin-like components

of cortical cytoskeletons, control the local curvature of biological membranes and hence cell shape in static and dynamic conditions—is relevant not only to RBCs but also to all cellular systems with adsorbed networks of spectrin or spectrin-like filaments, such as neurons [50] and intracellular organelles [62].

Appendix Curling Ghosts

A1. Derivation of the Curvature Force on the Membrane

We derive the forces at the membrane, by treating it as a "one-dimensional membrane," that is, a thin strip of width w, with a bending modulus and tension coefficient. The Helfrich free energy of this membrane is given in Eq. (A7) and is used to derive the local restoring forces by the usual variation method. The derivation given below gives the details of this variation and is a one-dimensional version of the more general derivation given in Refs. [46,58].

Since the overall contour length is not constant in our system, the variation of the coordinates has to be taken with respect to their absolute index u along the contour, which is constant. In these terms, the curvature H appearing in the Helfrich free energy [59] is written as (standard differential geometry) x'

$$H = \frac{\dot{x}\ddot{y} - \ddot{x}\dot{y}}{\sqrt{\dot{x}^2 + \dot{y}^2}^3}, \tag{A1}$$

where the $\cdot$ symbol denotes differentiation with respect to the index of the point along the contour and the free energy is

$$\mathcal{F} = w \int^1 \left(\frac{1}{2}\kappa H^2 + \sigma\right) \sqrt{\dot{x}^2 + \dot{y}^2}\,\mathrm{d}u, \tag{A2}$$

where $\mathrm{d}s/\mathrm{d}u = \dot{s} = \sqrt{\dot{x}^2 + \dot{y}^2}$. The variation of this free energy gives the forces, for example, in the x-direction:

$$F_x = -\frac{\delta \mathcal{F}}{\delta x} = \frac{\mathrm{d}}{\mathrm{d}u}\frac{\partial \mathcal{F}}{\partial \dot{x}} - \frac{\mathrm{d}^2}{\mathrm{d}u^2}\frac{\partial \mathcal{F}}{\partial \ddot{x}}. \tag{A3}$$

The resulting equation of motion from this variation gives very long expressions that are not amenable to easy analysis, although they can be used for the numerical simulations.

To arrive at simpler expressions, we will develop the terms in Eq. (A3) and simplify at the end by assuming that the arc-length separation between the nodes along the contour are all the same. This is maintained as the simulation progresses by using the spline routine to rediscretize evenly the contour as its length evolves.

The first term on the RHS of Eq. (A3) is

$$\frac{\partial \mathcal{F}}{\partial \dot{x}} = H^2 \frac{\partial x}{\partial s} + 2H \frac{\partial H}{\partial \dot{x}} \dot{s}, \tag{A4}$$

where $\partial \dot{s}/\partial \dot{x} = \dot{x}/\sqrt{\dot{x}^2 + \dot{y}^2} = \partial x/\partial s$:

$$\begin{aligned} \frac{\mathrm{d}}{\mathrm{d}u} \frac{\partial \mathcal{F}}{\partial \dot{x}} = {} & 2\dot{s} H H' x' + \dot{s} H^2 x'' + 2\dot{s}^2 H' \frac{\partial H}{\partial \dot{x}} \\ & + 2H \frac{\partial H}{\partial \dot{x}} \ddot{s} + 2H\dot{s}^2 \frac{\partial H'}{\partial \dot{x}}, \end{aligned} \tag{A5}$$

where $\partial H/\partial \dot{x} = \ddot{y}/\dot{s}^3 - 3x'H/\dot{s}$. We therefore need to find an expression for $\ddot{y}$ (and $\ddot{x}$) by using the definition of $H = (x'\ddot{y} - y'\ddot{x})/\dot{s}^2$ and $\ddot{s} = x'\ddot{x} + y'\ddot{y}$. The final expressions that we get are $\ddot{y} = \ddot{s}y' + \dot{s}^2 x' H$ and $\ddot{x} = \ddot{s}x' - \dot{s}^2 y' H$.

We now assume that $\dot{s}$ is independent of u, so that $\ddot{s} = \dddot{s} = \cdots = 0$. The last term in Eq. (A5) becomes

$$\frac{\partial H'}{\partial \dot{x}} = -\frac{2}{\dot{s}} \frac{\partial}{\partial s} (x'H). \tag{A6}$$

The second term on the RHS of Eq. (A3) is

$$\frac{\partial \mathcal{F}}{\partial \ddot{x}} = \frac{-2Hy'}{\dot{s}} \tag{A7}$$

and we get

$$\frac{\mathrm{d}^2}{\mathrm{d}u^2} \frac{\partial \mathcal{F}}{\partial \ddot{x}} = -2\dot{s} \frac{\partial^2}{\partial s^2} (Hy'). \tag{A8}$$

We now write H in terms of s as $H = \vec{H} \cdot \hat{n} = -x''y' + y''x'$, where $\vec{H} = x''\hat{x} + y''\hat{y}$ and $\hat{n} = -y'\hat{x} + x'\hat{y}$, so that

$$H' = -\gamma' x''' + x'\gamma''', \qquad H'' = -\gamma'' x''' + x''\gamma''' - \gamma' x^{(4)} + x'\gamma^{(4)}. \tag{A9}$$

There is another force contribution from the membrane tension, giving a term of the form $F_x \propto \dot{s}x''$, so in the normal direction we get $F_{\mathrm{n}} = \dot{s}\sigma(-\gamma' x'' + x'\gamma'') = \dot{s}\sigma H$?, where we used the identity $x'^2 + \gamma'^2 = 1$ and therefore $2(x'x'' + \gamma'\gamma'') = \partial\,(x'^2 + \gamma'^2)/\partial\, s = 0$.

Putting everything together, the normal force acting on the membrane due to curvature and tension is

$$F = \overrightarrow{F}\cdot\hat{n} = -\gamma' F_x + x' F_\gamma \tag{A10}$$

$$= \dot{s}\frac{1}{2}\kappa\left(-2\nabla^2 H - 2H\left(\gamma'\gamma^3 + x'x^3\right) - 3\left(\overrightarrow{H}\cdot\hat{n}\right)^3\right) + \dot{s}\sigma H \tag{A11}$$

$$= \dot{s}\kappa\left(-\nabla^2 H - \frac{1}{2}\left(\overrightarrow{H}\cdot\hat{n}\right)^3\right) + \dot{s}\sigma H$$

$$= \dot{s}\frac{1}{2}\kappa\left(2\left(\gamma' x^{(4)} - x'\gamma^{(4)}\right) - 3\left(\overrightarrow{H}\cdot\hat{n}\right)^3\right) + \dot{s}\sigma H,$$

where we used the identity $x'^2 + \gamma'^2 = 1$ and therefore $2(x'x'' + \gamma'\gamma'') = \partial\,(x'^2 + \gamma'^2)/\partial s = 0$ and $(\gamma'\gamma^3 + x'x^3) = -\,(x''^2 + \gamma''^2) = -\,H^2$. These expressions are identical to those derived in Refs. [42,43].

Since the forces are per unit length, while we calculated above the forces per unit u, so we divide by $\dot{s}$ and finally get

$$F_{\mathrm{n}} = \kappa\left(\left(\gamma' x^{(4)} - x'\gamma^{(4)}\right) - \frac{3}{2}H^3\right) + \sigma H. \tag{A12}$$

A1.1. Proteins with Spontaneous Curvature

When there are proteins with spontaneous curvature, the free energy (Eq. A2) changes to

$$\mathcal{F} = w\int^1 \left(\frac{1}{2}\kappa(H + \bar{H}n)^2 + (\sigma - \alpha n)\right)\sqrt{\dot{x}^2 + \dot{\gamma}^2}\,\mathrm{d}u, \tag{A13}$$

where n is the density of proteins along the contour, which may not be uniform. Expanding the quadratic term, we get $H^2 + 2H\bar{H}n + (\bar{H}n)^2$?.

The variation of the first term was done above (all the variations are of the integrand times the $\dot{s}$ factor).

The new contributions to the forces acting on the membrane are (normal force per unit length)

$$\begin{aligned} F_{\text{spon,n}} &= \overrightarrow{F}_{\text{spon}} \cdot \hat{n} = -\gamma' F_{\text{spon},x} + x' F_{\text{spon},\gamma} \\ &= \frac{\kappa}{2}\left((\bar{H}n)^2 H + 2(\bar{H}n'')\right) \end{aligned} \tag{A14}$$

and

$$F_{\text{tension,n}} = \overrightarrow{F}_{\text{spon}} \cdot \hat{n} = -\alpha n H. \tag{A15}$$

A1.2. Fluxes and Diffusion of the Proteins

The conservation equation for the proteins, along the contour [42], becomes

$$\frac{1}{\dot{s}}\frac{\partial \dot{s}n}{\partial t} = \frac{D}{\dot{s}}\nabla_{\text{s}}^2(\dot{s}n) + \frac{1}{\dot{s}}\frac{\Lambda}{n_{\text{s}}}\nabla_{\text{s}}\left(\dot{s}n\nabla_{\text{s}}\left(\frac{1}{\dot{s}}\frac{\delta E}{\delta n}\right)\right), \tag{A16}$$

where the number of proteins in each unit contour length is $N = \dot{s}nn_{\text{s}}$ (n_{s} is the saturation concentration of the proteins), E is the energy functional of Eq. (A13), and the derivative along the contour is $\nabla_{\text{s}} = \nabla_{\text{u}}/\dot{s}$. We therefore get

$$\frac{\partial n}{\partial t} + \frac{n}{\dot{s}}\frac{\partial \dot{s}}{\partial t} = \frac{D}{\dot{s}}\nabla_{\text{s}}^2(\dot{s}n) + \frac{D}{k_{\text{B}}Tn_{\text{s}}\dot{s}^2}\nabla_{\text{u}}\left(n\nabla_{\text{u}}\frac{\delta e}{\delta n}\right), \tag{A17}$$

where e is the energy per unit length, that is, the integrand in Eq. (A13) with respect to ds.

If the number of proteins is conserved, even though we allow the membrane overall length to change, then Eq. (A17) is correct. If however there is a reservoir of membrane that allows it to change in length, then this membrane can include lipids and proteins, so that the total number of proteins is not conserved when the membrane length changes. In this case, the change in the density due to length changes is removed, assumed to be balanced by the currents into/out of the reservoir. Equation (A17) is then modified by removing the second term on the left-hand side.

In our calculation of osteointegration, a nonlinear tension was employed, and as a result, the length of each membrane segment changed very little, so the second term on the LHS of Eq. (A17) was neglected.

A2. Numerical Realization of the Model

A2.1. Discretization of the Model

Since the flat shape model represents a segment of the whole cell, we used periodic boundary conditions. Thus, the number of grid points N equals the number of discretizations. In our model, the density n of element i is given by

$$n_i = \frac{N_i}{\Delta s_i}. \tag{A18}$$

A2.2. The Boundary Conditions

We employed periodic boundary conditions. The calculation of the first and second derivatives of the function along the x-direction was performed using the following explicit Euler method:

$$\begin{aligned} \frac{\partial x}{\partial s} &= \frac{x_{n+1} - x_{n-1}}{2\Delta s_n}, \\ \frac{\partial^2 x}{\partial s^2} &= \frac{x_{n-1} - 2x_n + x_{n+1}}{\Delta s_n^2}, \end{aligned} \tag{A19}$$

where the subscripts n, $n + 1$, and $n - 1$ represent the current, next, and previous nodes, respectively. The derivatives of the function along the y-direction were calculated in a similar manner. For the calculations of derivatives of the first point, the last point was added before it; while for the calculation of derivatives of the last point, the first point was added after it.

A2.3. The Variation of the Helfrich Equation

To find the slowest optimal projectile with the lowest energy of the membrane, we found the variation of the energy equation along the x and y coordinates, $\delta F/\delta x$ and $\delta F/\delta y$, respectively.

Our derivation as described above was verified using Mathematica software. The projected normal force along the x- and y-axes is

$$\begin{aligned} F_x &= F_{\mathrm{n}}\left(-\frac{\partial y}{\partial s}\right), \\ F_y &= F_{\mathrm{n}}\left(\frac{\partial x}{\partial s}\right), \end{aligned} \tag{A20}$$

where F_x and F_y are the projected forces along the x- and y-directions, respectively. The time evolution of the x and y coordinates is given by

$$\begin{aligned} x_i &= x_i - \Delta t\left(1/2\kappa F_{x,i}\right)/\xi, \\ y_i &= y_i - \Delta t\left(1/2\kappa F_{y,i}\right)/\xi, \end{aligned} \tag{A21}$$

where $F_{x,i}$ and $F_{y,i}$ are contributions of the variation along the x and y coordinates, at index i, and ξ is the friction coefficient, which takes into account drag forces by the surrounding medium. The energy contributions $F_{x,i}$ and $F_{y,i}$ were taken only at the normal direction. Therefore, the membrane dynamics due to the energy minimization was constrained only in the normal direction.

A3. Analytic Derivation of the Steady-State Solution

We derive the steady-state solution in order to shed light on the underlying mechanisms responsible for the observed steady-state shape. In a steady state, the sum of fluxes of membrane-bound protein complexes (PCs) is equal to zero. In particular, the sum of the attraction flux due to membrane intrinsic curvature, J_{curv}, and the dispersion flux, J_{disp}, gives

$$\frac{\kappa\Lambda\bar{H}}{n_{\mathrm{s}}}\left(\nabla H - \frac{\bar{H}}{n_{\mathrm{s}}}\nabla n\right) = 0. \tag{A22}$$

The nontrivial solution is

$$\nabla n = \frac{n_{\mathrm{s}}}{\bar{H}}\nabla H, \tag{A23}$$

where H is $\nabla^2 h$. By integrating both sides of Eq. A23 we get

$$n(x) = \frac{\nabla^2 h}{\bar{H}} + n_0. \tag{A24}$$

The function representing the peak region at the steady state is approximated up to a fourth-order polynomial. Note that due to symmetry around the peak as observed in numerical simulations, the odd orders of the polynomial are assumed to be zero. We use the proportionality found from Eq. A24 to obtain the shape function, $h(x)$, and the distribution of PCs, $n(x)$, as follows:

$$\begin{aligned} h(x) &= h + fx^2 + gx^4, \\ n(x) &= n_0 + 2f\frac{n_{\mathrm{s}}}{\bar{H}} + \frac{n_{\mathrm{s}}}{\bar{H}}gx^2, \end{aligned} \tag{A25}$$

where x is the length along the x-axis. The following is the sum of forces F_{tot} derived from the free energy (Eq. (A13)):

$$F_{\text{tot}} = \kappa\left(-\nabla^2 H + \bar{H}\nabla^2 n + \frac{1}{2}n^2\bar{H}^2 H - \frac{1}{2}H^3\right) + (\sigma - \alpha n)H - 2\gamma h. \tag{A26}$$

We find the steady-state analytic solutions for Eq. (A26). The aim is to have a better understanding of how changes in α impact on the SS shape and distribution of PCs. The steady states $n(x)$ and $h(x)$ (Eq. (A25)) were incorporated into the force equation (Eq. (A26)). After incorporating these two functions, we look for a solution that vanishes all the coefficients of zeroth-, second-, and fourth-order terms. The result of this system of equations is the solution for the three unknown functions: f, g, and h. The following is the list of parameter values used in this derivation: $\alpha = 0.05\ \text{g s}^{-2}$, $\gamma = 0.00004\ \text{g s}^{-2}$, $n_0 = 0.1$ (which is the initial relative density of PCs), $n_{\text{sat}} = 10\ \mu\text{m}^{-2}$, $\kappa = 100 k_{\text{B}}T$, $\bar{H} = -10\,\mu\text{m}^{-1}$, and $\sigma = 0.001\ \text{g s}^{-2}$.

The first solution is the trivial solution with unknowns equal zero and the second solution is $h(x) > 0$, $g(x) < 0$, and $f(x) < 0$. The plot of this solution with respect to x gives a similar shape to the steady states seen in numerical simulations. From the approximation in (Eq. (A25)), the value of $1/\sqrt{f}$ can be derived to give the width of $h(x)$. We will next determine which parameter has the largest effect on the width of $h(x)$. From our analytic derivation, we obtain that

$$f_\alpha = \frac{-\bar{H}\left(2(\sigma - n_0\alpha) + \bar{H}^2 n_0^2 \kappa\right)}{16\left(\alpha - \bar{H}^2 n_0 \kappa\right)}, \tag{A27}$$

whereby neglecting the terms with κ due to their smaller magnitude yields:

$$f_\alpha \simeq \bar{H}\frac{n_0\alpha - \sigma}{8\alpha}. \tag{A28}$$

We find that the proportionality of the width is

$$1/\sqrt{f} = \sqrt{\frac{8\alpha}{\bar{H}(\sigma - n_0\alpha)}}. \tag{A29}$$

The following correlations are gleaned from Eq. (A29). Given a large adhesion constant (α) due to stronger adhesion to the extracellular matrix, the width of $h(x)$ is smaller to result in a sharper tip.

REFERENCES

[1] V. Bennett, The spectrin–actin junction of erythrocyte membrane skeletons, Biochim. Biophys. Acta 18 (1989) 107–121.

[2] A. Iglic, A possible mechanism determining the stability of spiculated red blood cells, J. Biomech. 30 (1997) 35–40.

[3] A. Iglic, V. Kralj-Iglic, H. Hagerstrand, Amphiphile induced echinocyte–spheroechinocyte red blood cell shape transformation, Eur. Biophys. J. 27 (1998) 335–339.

[4] A. Iglic, V. Kralj-Iglic, H. Hagerstrand, Stability of spiculated red blood cells induced by intercalation of amphiphiles in cell membrane, Med. Biol. Eng. Comput. 36 (1998) 251–255.

[5] H. Hagerstrand, M. Danieluk, M. Bobrowska-Hagerstrand, A. Iglic, A. Wrobel, B. Isomaa, M. Nikinmaa, Influence of band 3 protein absence and skeletal structures on amphiphile- and Ca^{2+}-induced shape alterations in erythrocytes: a study with lamprey (*Lampetra fluviatilis*), trout (*Oncorhynchus mykiss*) and human erythrocytes, Biochim. Biophys. Acta 1466 (2000) 125–138.

[6] V.L. Lew, A. Hockaday, R.M. Bookchin, Mechanism of spontaneous inside-out vesiculation of red cell membranes, J. Cell Biol. 106 (1988) 1893–1901.

[7] V.L. Lew, S. Muallem, C.A. Seymour, Properties of the Ca^{2+}-activated K channel in one-step inside-out vesicles from human red cell membranes, Nature 296 (1982) 742–744.

[8] T.L. Steck, R.S. Weinstein, D.F. Wallach, Inside-out red cell membrane vesicles: preparation and purification, Science 168 (1970) 255–257.

[9] T. Tiffert, A.R. Hockaday, V.L. Lew, Cytoskeletal protein changes and morphology during spontaneous inside-out vesiculation of human red cell membranes, J. Physiol. 487 (1995) 99.

[10] A. Duran, E. Cabib, B. Bowers, Chitin synthetase distribution on the yeast plasma membrane, Science 203 (1979) 363–365.

[11] B.E. Burke, D.M. Shotton, Erythrocyte membrane skeleton abnormalities in hereditary spherocytosis, Br. J. Haematol. 54 (1983) 173–187.

[12] J.M. Gluck, M. Wittlich, B.W. Koening, Integral membrane proteins in nanodiscs can be studied by solution NMR spectroscopy, J. Am. Chem. Soc. 131 (2009) 12060–12061.

[13] J. Zimmerberg, M.M. Kozlov, How proteins produce cellular membrane curvature, Nat. Rev. Mol. Cell Biol. 7 (2006) 9–19.

[14] A. Hagerstrand, L. Mrowczynska, U. Salzer, R. Prohaska, A.K. Michelsenn, V. Kralj-Iglic, et al. Curvature dependent lateral distribution of raft markers in the human erythrocyte membrane, Mol. Membr. Biol. 23 (2006) 277–288.

[15] A. Iglic, M. Lokar, B. Babnik, T. Slivnik, P. Veranic, H. Hgerstrand, V. Kralj-Iglic, Possible role of flexible red blood cell membrane nanodomains in the growth and stability of membrane nanotubes, Blood Cells Mol. Dis. 39 (2007) 14–23.

[16] A. Iglic, T. Slivnik, V. Kralj-Iglic, Elastic properties of biological membranes influenced by attached proteins, J. Biomech. 40 (2007) 2492–2500.

[17] J. Jorgacevski, M. Fosnaric, N. Vardjan, M. Stenovec, M. Potokar, M. Kreft, et al. Fusion pore stability of peptidergic vesicles, Mol. Member. Biol. 27 (2010) 65–80.

[18] Š. Perutkova, V. Kralj-Iglic, M. Frank, A. Iglic, Mechanical stability of membrane nanotubular protrusions influenced by attachment of flexible rod-like proteins, J. Biomech. 43 (2010) 1612–1617.

[19] D. Kabaso, R. Shlomovitz, T. Auth, V.L. Lew, N.S. Gov, Curling and local shape changes of red blood cell membranes driven by cytoskeletal reorganization, Biophys. J. 99 (2010) 88.

[20] D.M. Shotton, The proteins of the erythrocyte membrane, in: J.R. Harris (Ed.), Electron Microscopy of Proteins, vol. 4. Academic Press, London, 1983, pp. 205–330.
[21] T.L. Steck, J.A. Kant, Preparation of impermeable ghosts and inside-out vesicles from human erythrocyte membranes, Methods Enzymol. 31 (1974) 172–180.
[22] N.S. Gov, Active elastic network: cytoskeleton of the red blood cell, Phys. Rev. E Stat. Nonlin. Soft Matter Phys. 75 (2007) 011921.
[23] J. Li, G. Lykotrafitis, S. Suresh, Cytoskeletal dynamics of human erythrocyte, Proc. Natl. Acad. Sci. USA 104 (2007) 4937–4942.
[24] C. Frank, H. Frielinghaus, D. Richter, Hydrophilic alcohol ethoxylates as efficiency boosters for microemulsions, Langmuir 24 (2008) 6036–6043.
[25] V. Nikolov, R. Lipowsky, R. Dimova, Behavior of giant vesicles with anchored DNA molecules, Biophys. J. 92 (2007) 4356–4368.
[26] I. Tsafrir, Y. Caspi, J. Stavans, Budding and tubulation in highly oblate vesicles by anchored amphiphilic molecules, Phys. Rev. Lett. 91 (2003) 138102.
[27] I. Tsafrir, D. Sagi, T. Arzi, J. Stavans, Pearling instabilities of membrane tubes with anchored polymers, Phys. Rev. Lett. 86 (2001) 1138–1141.
[28] T. Auth, G. Gompper, Self-avoiding linear and star polymers anchored to membranes, Phys. Rev. E Stat. Nonlin. Soft Matter Phys. 68 (2003) 051801.
[29] E. Eisenriegler, A. Hanke, S. Dietrich, Polymers interacting with spherical and rodlike particles, Phys. Rev. E 54 (1996) 1134–1152.
[30] R. Lipowsky, Flexible membranes with anchored polymers, Colloids Surf. A Physicochem. Eng. Asp. 128 (1997) 255–264.
[31] T. Auth, N.S. Gov, S.A. Safran, Filament networks attached to membranes: cytoskeletal pressure and local bilayer deformation, N. J. Phys. 9 (2007) 430.
[32] T. Auth, G. Gompper, Self-avoiding linear and star polymers anchored to membranes, Phys. Rev. E 68 (2003) 051801.
[33] T. Auth, S.A. Safran, N.S. Gov, Fluctuations of coupled fluid and solid membranes with application to red blood cells, Phys. Rev. E Stat. Nonlin. Soft Matter Phys. 76 (2007) 051910.
[34] N.S. Gov, S.A. Safran, Red blood cell membrane fluctuations and shape controlled by ATP-induced cytoskeletal defects, Biophys. J. 88 (2005) 1859–1874.
[35] R. Podgornik, Surface polymer network model and effective membrane curvature elasticity, Phys. Rev. E Stat. Phys. Plasmas Fluids Relat. Interdiscip. Topics 51 (1995) 3368–3375.
[36] S.C. Liu, L.H. Derick, J. Palek, Visualization of the hexagonal lattice in the erythrocyte membrane skeleton, J. Cell Biol. 104 (1987) 527–536.
[37] Y. Takakuwa, N. Mohandas, Modulation of erythrocyte membrane material properties by Ca^{2+} and calmodulin. Implications for their role in regulation of skeletal protein interactions, J. Clin. Invest. 82 (1988) 394–400.
[38] F. Liu, H. Mizukami, A. Ostafin, Calcium-dependent human erythrocyte cytoskeleton stability analysis through atomic force microscopy, J. Struct. Biol. 150 (2005) 200–210.
[39] T. Auth, G. Gompper, Budding and vesiculation induced by conical membrane inclusions, Phys. Rev. E Stat. Nonlin. Soft Matter Phys. 80 (2009) 031901–031910.
[40] M. Breidenich, R.R. Netz, R. Lipowsky, The shape of polymer-decorated membranes, Europhys. Lett. 49 (2000) 431–437.
[41] W. Helfrich, Elastic properties of lipid bilayers: theory and possible experiments, Z. Naturforsch. C 28 (1973) 693–703.
[42] R. Lipowsky, The conformation of membranes, Nature 349 (1991) 475–481.
[43] Z.C. Tu, Z.C. Ou-Yang, Lipid membranes with free edges, Phys. Rev. E Stat. Nonlin. Soft Matter Phys. 68 (2003) 061915.
[44] U. Seifert, K. Berndl, R. Lipowsky, Shape transformations of vesicles: phase diagram for spontaneous-curvature and bilayer coupling models, Phys. Rev. A 44 (1991) 1182–1202.

[45] A. Veksler, N.S. Gov, Phase transitions of the coupled membrane–cytoskeleton modify cellular shape, Biophys. J. 93 (2007) 3798–3810.
[46] E. Mabrouk, D. Cuvelier, M.H. Li, Bursting of sensitive polymersomes induced by curling, Proc. Natl. Acad. Sci. USA 106 (2009) 7294–7298.
[47] J.A. Dvorak, L.H. Miller, T. Shiroishi, Invasion of erythrocytes by malaria merozoites, Science 187 (1975) 748–750.
[48] P.R. Gilson, B.S. Crabb, Morphology and kinetics of the three distinct phases of red blood cell invasion by *Plasmodium falciparum* merozoites, Int. J. Parasitol. 39 (2009) 91–96.
[49] S. Glushakova, D. Yin, J. Zimmerberg, Membrane transformation during malaria parasite release from human red blood cells, Curr. Biol. 15 (2005) 1645–1650.
[50] L. Lencesova, A. O'Neill, M.P. Blaustein, Plasma membrane–cytoskeleton–endoplasmic reticulum complexes in neurons and astrocytes, J. Biol. Chem. 23 (2004) 2885–2893.
[51] V.L. Lew, T. Tiffert, Is invasion efficiency in malaria controlled by pre-invasion events? Trends Parasitol. 23 (2007) 481–484.
[52] M.H. Grati, M.E. Schneider, B. Kachar, Rapid turnover of stereocilia membrane proteins: evidence from the trafficking and mobility of plasma membrane Ca^{2+}-ATPase 2, J. Neurosci. 26 (2006) 6386–6395.
[53] V.L. Lew, N. Daw, T. Tiffert, Distribution of plasma membrane Ca^{2+} pump activity in normal human red blood cells, Blood 102 (2003) 4206–4213.
[54] J.J. Blum, G. Lawler, I. Shin, Effect of cytoskeletal geometry on intracellular diffusion, Biophys. J. 56 (1989) 995–1005.
[55] C. Gelhaus, R. Vicik, T. Schirmeister, M. Leippe, Blocking effect of a biotinylated protease inhibitor on the egress of *Plasmodium falciparum* merozoites from infected red blood cells, Biol. Chem. 386 (2005) 499–502.
[56] S. Glushakova, J. Mazar, M.F. Hohmann-Marriott, E. Hama, J. Zimmerberg, Irreversible effect of cysteine protease inhibitors on the release of malaria parasites from infected erythrocytes, Cell. Microbiol. 11 (2009) 95–105.
[57] R. Chandramohanadas, P.H. Davis, D.P. Beiting, M.B. Harbut, C. Darling, G. Velmourougane, et al. Apicomplexan parasites co-opt host calpains to facilitate their escape from infected cells, Science 324 (2009) 794–797.
[58] M. Treeck, S. Zacherl, T.W. Gilberger, Functional analysis of the leading malaria vaccine candidate AMA-1 reveals an essential role for the cytoplasmic domain in the invasion process, PLoS Pathog. 5 (2009) e1000322.
[59] A.R. Dluzewski, D. Zicha, W.B. Gratzer, Origins of the parasitophorous vacuole membrane of the malaria parasite: surface area of the parasitized red cell, Eur. J. Cell Biol. 68 (1995) 446–449.
[60] J. Olson, A. Kilejian, Involvement of spectrin and ATP in infection of resealed erythrocyte ghosts by the human malaria parasite, *Plasmodium falciparum*, J. Cell Biol. 95 (1982) 757–762.
[61] T. Tiffert, V.L. Lew, N. Mohandas, The hydration state of human red blood cells and their susceptibility to invasion by *Plasmodium falciparum*, Blood 105 (2005) 4853–4860.
[62] M. De Matteis, J. Morrow, Spectrin tethers and mesh in the biosynthetic pathway, J. Cell Sci. 113 (2003) 2331–2343.